Microfluidics and Nanofluidics (2019) 23:125
https://doi.org/10.1007/s10404-019-2292-0

RESEARCH PAPER

Particle separation in xanthan gum solutions

Di Li[1] · Xingchen Shao[1] · Joshua B. Bostwick[1] · Xiangchun Xuan[1]

Received: 9 August 2019 / Accepted: 4 October 2019

Abstract
Label-free separation of particles by an intrinsic property can be implemented in microfluidic devices through either an externally imposed field or an inherent flow-induced force. Among the latter type of passive techniques, elastic or elasto-inertial lift-based particle separation in non-Newtonian fluids has received a rapidly growing interest in the past decade. However, current demonstrations of particle separation in non-Newtonian fluids have all taken place in viscoelastic polymer or biological solutions. We demonstrate for the first time a continuous sheath-free separation of polystyrene particles in the flow of weakly elastic xanthan gum (XG) solution through a simple straight rectangular microchannel. This separation is fundamentally different from that in the flow of viscoelastic solutions. We explain the observed particle migrations in XG solutions using the competition of a strong wall-directed (because of the strong shear thinning effect) and a small center-directed (because of the weak elasticity effect) lateral force induced by normal stresses in a Poiseuille flow.

Keywords Particle separation · Lateral migration · Lift force · Shear thinning · Elasticity · Microfluidics

1 Introduction

Separating particles by an extrinsic label (e.g., fluorescence tag) or an intrinsic property (e.g., size) is important to many biological, chemical, and environmental applications (Gossett et al. 2010; Sajeesh and Sen 2014). Label-free particle separation has been demonstrated in continuous-flow microfluidic devices through a variety of field-driven techniques, which may be classified as active or passive depending on the nature of the associated force(s) (Karimi et al. 2013; Tang et al. 2019). The active separation uses an external field, e.g., acoustic (Wu et al. 2019), electric (Lapizco-Encinas 2019), or magnetic (Munaz et al. 2018), to exert a force on the suspended particles in a fluid flow. This type of techniques is capable of separating particles at a high resolution with a high specificity, but at the cost of limited throughput (Yan et al. 2017). In contrast, the passive separation exploits the inherent flow-induced hydrodynamic force to manipulate particles towards property-dependent equilibrium positions (Liu and Hu 2017). There has been a rapidly growing interest in the use of inertial (in Newtonian fluids) (Martel and Toner 2014; Amini et al. 2014; Zhang et al. 2016) and/or elastic (in non-Newtonian fluids) (Lu et al. 2017; Tian et al. 2019) forces for label-free separation of particles. Such a nonlinear microfluidic approach is envisioned to have potentials for the development of point-of-care devices (Stoecklein and Di Carlo 2019).

Current demonstrations of particle separation in non-Newtonian fluids have exclusively used polymer solutions or biological fluids that exhibit viscoelastic behaviors (D'Avino et al. 2017; Yuan et al. 2018). Among the various polymer solutions, polyethylene oxide (PEO) solution has a medium elasticity and a weak shear thinning (Rodd et al. 2005). PEO-based particle separation can be implemented with or without a sheath-flow focusing. For the former, if the particle-free sheath fluid is Newtonian, only the larger particles of the mixture in a PEO solution can migrate across the interface between the two fluids (Ha et al. 2016; Yuan et al. 2017a) because of the particle size-dependent viscoelastic force (Yuan et al. 2016a). If the sheath fluid uses the same PEO solution as the particle suspension, particles migrate towards size (Nam et al. 2012; Lu and Xuan 2015a; Zhou et al. 2019) and shape (Lu and Xuan 2015b) dependent

This article is part of the topical collection "Particle motion in non-Newtonian microfluidics" guest edited by Xiangchun Xuan and Gaetano D'Avino.

Electronic supplementary material The online version of this article (https://doi.org/10.1007/s10404-019-2292-0) contains supplementary material, which is available to authorized users.

✉ Xiangchun Xuan
xcxuan@clemson.edu

[1] Department of Mechanical Engineering, Clemson University, Clemson, SC 29634-0921, USA

Published online: 17 October 2019

lateral positions. Alternatively, the mixture of particles may be suspended in a Newtonian fluid that is pinched by a particle-free PEO core flow from the middle (Tian et al. 2017). This setup forms two sharp interfaces that allow for the penetration of only the large particles into the PEO solution (Liu et al. 2017; Tian et al. 2018). PEO-based particle separation has also been implemented without a sheath-flow focusing, where larger particles can be elasto-inertially focused leaving smaller particles dispersed (Yang et al. 2011; Ahn et al. 2015). In straight rectangular microchannels with a high width/height ratio (Liu et al. 2015b; Lu et al. 2015; Li et al. 2016b, 2018) or curved microchannels (Lee et al. 2013; Liu et al. 2016; Yuan et al. 2016b, 2017b), particles are focused towards size and shape dependent equilibrium positions.

Polyvinylpyrrolidone (PVP) solution is strongly elastic with a negligible shear thinning effect (Yang et al. 2011). Its elasticity causes rigid particles to migrate towards the centerline or the corners, whichever is closer, in a straight square microchannel when the fluid inertia is negligible (Yang et al. 2012). In contrast, soft particles are pushed away from the channel corners by the deformability-induced wall lift force (Leal 1980). Under the combined action of elastic and inertial focusing, particles in the flow of PVP solution through a two-stage bifurcating microchannel are aligned in the cylindrical main-branch and then displaced in each rectangular side-branch at a size dependent rate (Nam et al. 2015a). Polyacrylamide (PAA) solution is strongly viscoelastic and shear thinning, exhibiting the second normal stress difference (Lim et al. 2014). Small particles that are suspended in an off-center focused PAA solution are carried towards the channel walls by the second normal stress difference-induced secondary flow (Villone et al. 2013), while large particles remain inside the focused PAA solution.

In addition, a couple of viscoelastic biological fluids have been demonstrated for passive particle separations. Hyaluronic acid (HA) solution has strong viscoelasticity and shear thinning (Haward et al. 2013). It can be used to replace the PVP solution (Nam et al. 2015a) for sheathless particle separation in a bifurcating microchannel with the advantages of significantly reduced pumping pressure and shear stress (on bioparticles) (Nam et al. 2015b). HA solution has also been used for high throughput malaria parasite separation in a revised bifurcating microchannel with a slit-like main-branch that can be fabricated in one layer (Nam et al. 2016). Moreover, the combined fluid elasticity and shear thinning effects of HA solution enable a sheath-free separation of particles by size in straight rectangular microchannels (Del Giudice et al. 2017; Nam et al. 2019). DNA solution is strongly viscoelastic because of the long relaxation time of DNA molecules. An extremely dilute λ-DNA solution, at which the fluid shear thinning effect is negligible, has been demonstrated to significantly improve the sheath-flow separation of rigid spherical particles (Kang et al. 2013). More recently, λ-DNA solution has been used as a viscoelastic carrier medium for bioparticle separation over a wide range of sizes (Liu et al. 2019).

In a recent study, Li and Xuan (2018) observed in a straight rectangular microchannel the lateral migration of rigid spherical particles in the flow of xanthan gum (XG) solution that is strongly shear thinning with little elasticity. The equilibrium particle positions in the XG solution are different from those in a Newtonian fluid or any of the viscoelastic solutions. Moreover, their locations are found to be a strong function of particle size (Li and Xuan 2019), which implies a potentially high throughput separation of particles in the flow of XG solutions through a straight rectangular microchannel. The aim of this work is to demonstrate the feasibility of such a continuous sheath- and label-free separation using both a binary and a ternary mixture of spherical polystyrene particles. A comprehensive parametric study is also performed for the binary particle separation.

2 Experiment

XG solutions (Tokyo Chemical Industry) were prepared in deionized water (Fisher Scientific) at 1000 ppm, 2000 ppm and 3000 ppm, respectively. The viscosity, η, was measured using a cone-plate rheometer (Anton Paar, MCR 302) over a wide range of shear rates at room temperature. The obtained viscosity data are comparable to those reported by Japper-Jaafar et al. (2010), and fitted using the Carreau–Yasuda model (Yasuda et al. 1981), as shown in Fig. 1:

$$\frac{\eta-\eta_\infty}{\eta_0-\eta_\infty}=\left[1+\left(\lambda_{CY}\dot{\gamma}\right)^a\right]^{(n-1)/a}, \tag{1}$$

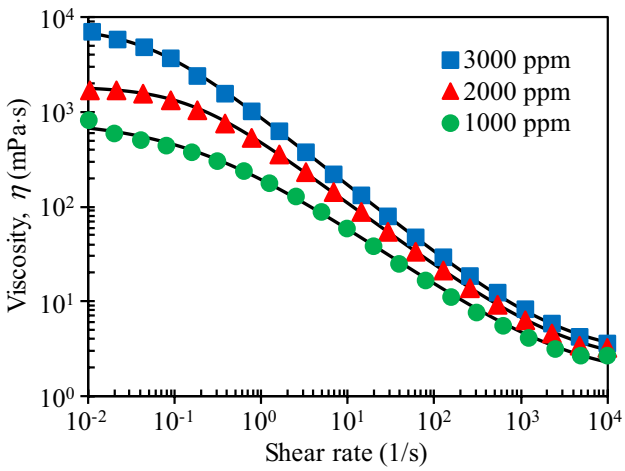

Fig. 1 Experimentally measured (symbols) and theoretically fitted (lines, via the Carreau–Yasuda model) viscosity data of the prepared XG solutions

Table 1 Summary of the parameters in the Carreau–Yasuda model [refer to Eq. (1) for the definitions of symbols] for fitting with the experimentally measured viscosity data (Fig. 1) of the prepared XG solutions

XG concentration (ppm)	n	η_0 (Pa•s)	η_∞ (Pa•s)	λ_{CY} (s)	a
1000	0.36	0.82	1.55×10^{-3}	5.62	0.57
2000	0.32	1.87	2.10×10^{-3}	6.62	1.02
3000	0.28	8.00	2.64×10^{-3}	20.00	0.94

where η_∞ is the infinite-shear-rate viscosity, η_0 is the zero-shear-rate viscosity, λ_{CY} is a time constant, $\dot{\gamma}$ is the fluid shear rate, a is a fitting parameter, and n is the power-law index. Table 1 presents the fitting values of the parameters in Eq. (1) for the three prepared XG solutions. All solutions are strongly shear thinning with the power-law index, n, decreasing at a higher concentration. We were unable to measure the fluid elasticity (e.g., relaxation time) of XG solutions due to the limitation of our equipment. While they were found in some studies to behave like polyelectrolyte solutions with elastic components (Zirnsak et al. 1999; Wyatt and Liberatore 2009), XG solutions have been more often reported in the literature to exhibit small elasticity effects (Dhahir and Walters 1989; Lindner et al. 2000; Aytouna et al. 2013; Haase et al. 2017). We thus assume in this work that XG solutions are weakly elastic fluids or at least their elasticity effect is much smaller than the shear thinning effect. Three types of spherical polystyrene particles were used: 5 µm red fluorescent (Magsphere), 10 µm green fluorescent (Thermo Scientific) and 15 µm plain (Sigma-Aldrich). The latter two particles were mixed and re-suspended in XG solutions (to a final concentration of 10^6–10^7 particles per milliliter each) for most of the tests. They were also mixed into water for a control experiment. All three particles were mixed in 2000 ppm XG solution for a demonstration of ternary particle separation. To reduce the particle aggregations and adhesions to channel walls, 0.1% Tween 20 (Fisher Scientific) was added to all the prepared particle suspensions.

Microchannels were fabricated with polydimethylsiloxane (PDMS) using the standard soft lithography technique described elsewhere (Li et al. 2016a). Each channel measured 65 µm wide and 2 cm long with depth that varied from 20 µm to 30 µm and 54 µm. At the end of each microchannel, there was a 900 µm-wide expansion for enhanced particle separation and visualization (Fig. 2a). A syringe pump (KD Scientific) was used to drive particle solutions through the microchannels. The motion of particles was recorded through an inverted fluorescent microscope (Nikon Eclipse TE2000U, Nikon Instruments) with a CCD camera (Nikon DS-Qi1Mc) at a rate of around 15 frames per second. As this fame rate was too low to obtain a clear view of individual particles along the straight channel, we focused our attentions primarily upon the outlet expansion, where the motion of particles was significantly slowed down. Fluorescent and bright field illuminations were used simultaneously to visualize both fluorescent (appearing bright or fluorescent if a color filter was in use) and plain (appearing dark) particles. Superimposed particle images were obtained using Nikon image software (NIS-Elements) by stacking frames with the maximum and minimum intensity projections for fluorescent and plain particles, respectively. Composite images were obtained by laying the superimposed image of plain particles over that of fluorescent ones after removing the background of the former. The probability distribution function (PDF) of each type of particles at the outlet expansion was analyzed using ImageJ software (National Institute of Health).

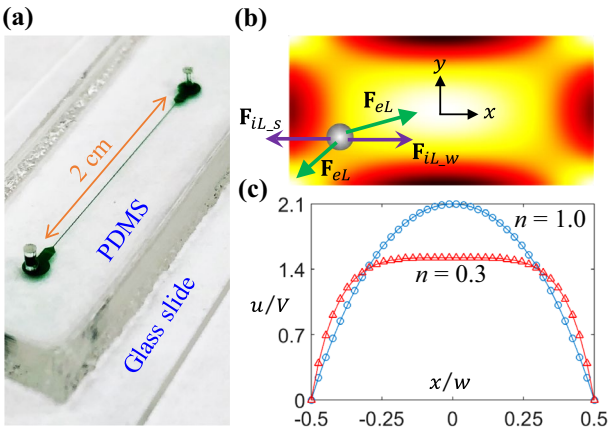

Fig. 2 **a** Isometric view of the fabricated microchannel in PDMS; **b** schematic illustration of the fluid rheology ($\boldsymbol{F}_{rL}$) and inertia ($\boldsymbol{F}_{iL}$) induced lateral forces acting on a particle in the flow of weakly elastic and strongly shear-thinning fluids through a straight rectangular microchannel. The background color shows the contour of fluid shear rate, $\dot{\gamma}$ (the darker the larger magnitude), at $n = 0.3$; **c** widthwise profile of the flow velocity (scaled by the average fluid velocity, V) for Newtonian ($n = 1.0$) and shear-thinning ($n = 0.3$) fluids in a 65 µm wide and 30 µm deep rectangular microchannel

3 Theory

A rigid particle experiences lateral forces in a confined flow of non-Newtonian fluids because of the fluid rheological and inertial effects (Leal 1980; D'Avino and Maffettone 2015). The fluid rheology-induced lateral force, $\boldsymbol{F}_{rL}$, results from normal stresses in a flow with a lateral variation of shear rate (Leal 1979). This rheological lift is usually considered proportional to the variation of the first normal stress difference, N_1, over the size of the particle in polymer solutions (Bird et al. 1987; Leshansky et al. 2007):

$$\boldsymbol{F}_{rL} \sim d^3 \nabla N_1, \tag{2}$$

where d is the particle diameter. Note that we use in this work the term rheological lift for strongly shear thinning and weakly elastic XG solutions instead of the traditional elastic (or viscoelastic) lift (Liu and Hu 2017; Lu et al. 2017; D'Avino et al. 2017; Yuan et al. 2018; Stoecklein and Di Carlo 2019) to avoid confusion. Like other diluted solutions of high molecular weight polymers (Barnes et al. 1989) N_1 of XG solutions, though small, also exhibits a power-law behavior (Escudier and Smith 1999; Won and Kim 2004), $N_1 = A\dot{\gamma}^m$, where A and m $(1 < m \leq 2)$ are both fluid-dependent constants. Thus, Eq. (2) is rewritten as

$$\boldsymbol{F}_{\mathrm{rL}} \sim d^3 A \nabla \dot{\gamma}^m. \tag{3}$$

As illustrated in Fig. 2b, $\boldsymbol{F}_{\mathrm{rL}}$ directs particles towards the low shear rate regions, i.e., the center and four corners of the channel cross section. In this schematic plot, the background color shows the contour of fluid shear rate, $\dot{\gamma}$ (the darker the larger magnitude), which was obtained from a 3D numerical simulation of the flow of XG solution in a 65 μm wide and 30 μm deep rectangular microchannel using COMSOL®. The fluid inertia-induced lateral force, $\boldsymbol{F}_{\mathrm{iL}}$, can be conveniently broken down into two components (Fig. 2b). The wall-induced inertial lift $\boldsymbol{F}_{\mathrm{iL\_w}}$, pushes particles away from any channel walls. The shear gradient-induced inertial lift, $\boldsymbol{F}_{\mathrm{iL\_s}}$, directs particles towards the center of each face of the microchannel (Ho and Leal 1974). The total inertial lift scales as (Asmolov 1999):

$$\boldsymbol{F}_{\mathrm{iL}} = \boldsymbol{F}_{\mathrm{iL\_w}} + \boldsymbol{F}_{\mathrm{iL\_s}} \sim \rho d^4 \dot{\gamma}^2 / D_{\mathrm{h}}^2, \tag{4}$$

where ρ is the fluid density, and D_{h} is the hydraulic diameter of the microchannel. This force directs particles towards multiple symmetric equilibrium positions in a straight rectangular microchannel that are at the centers of the channel faces (Amini et al. 2014; Zhang et al. 2016). More specifically, particles are inertially focused to the center of each long face in a high-aspect-ratio [defined in Eq. (6)] rectangular channel (Liu et al. 2015a).

The rheological and inertial lift forces are each a strong function of the fluid shear rate $\dot{\gamma}$, and hence, both affected by the fluid velocity profile that varies significantly with the power-law index (Fig. 2c, where the line plots were obtained from a 3D simulation of the XG and water flows in a 65 μm wide and 30 μm deep rectangular microchannel using COMSOL®). Therefore, we expect the equilibrium particle positions in strongly shear-thinning and weakly elastic XG solutions to be different from those in Newtonian or viscoelastic solutions. The flow rate effect on particle separation is studied in terms of the (channel) Reynolds number:

$$\mathrm{Re} = \frac{\rho V D_{\mathrm{h}}}{\eta} = \frac{2\rho Q}{\eta\left(\bar{\dot{\gamma}}\right)(w+h)}, \tag{5}$$

where V is the average fluid velocity, $\eta\left(\bar{\dot{\gamma}}\right)$ is the fluid viscosity estimated via Eq. (1) using the average fluid shear rate, $\bar{\dot{\gamma}} = 2V/w$, across the width, w, of the microchannel, Q is the volumetric flow rate, and h is the channel depth. The shear thinning effect on particle separation is studied in terms of the power-law index n, which is directly related to the XG concentration. The channel depth effect is studied in terms of the aspect ratio:

$$\mathrm{AR} = w/h. \tag{6}$$

4 Results and discussion

4.1 Binary particle separation

Figure 3 demonstrates a continuous separation of 10 μm (fluorescent) and 15 μm (plain) particles in the flow of 2000 ppm XG solution through a 65 μm wide and 30 μm deep straight rectangular microchannel (i.e., aspect ratio, AR = 2.2). The flow rate is 2.0 mL/h with a calculated Re = 3.7. Both types of particles travel into the microchannel uniformly as viewed from the snapshot image at the channel inlet. They, however, travel out of the channel along different flow paths; 15 μm particles tightly line each

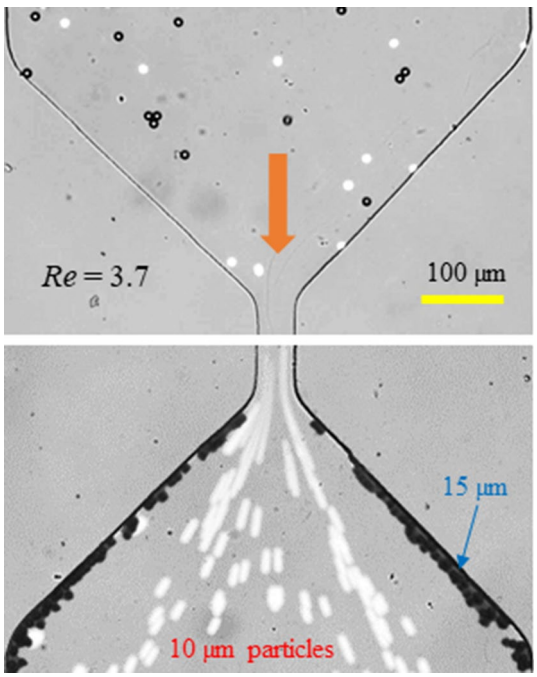

Fig. 3 Continuous sheath-free separation of 10 μm fluorescent (bright) and 15 μm plain (black) particles in 2000 ppm XG solution through a 65 μm wide and 30 μm deep microchannel at a flow rate of 2.0 mL/h (upper panel: snapshot image at the channel inlet; lower panel: composite image at the channel outlet). The block arrow indicates the flow direction

sidewall leaving nearly all 10 μm particles in the bulk of the channel expansion with no apparent equilibrium positions. Such a size-based sheathless particle separation does not take place in a Newtonian fluid (Fig. S-1) or a viscoelastic non-shear-thinning PVP solution, where the large and small particles both migrate towards the centerline (Li et al. 2016b). This separation is fundamentally different from that in the flow of viscoelastic and weakly shear-thinning PEO solution, where the larger particles migrate towards two off-center equilibrium positions with the smaller ones travelling between them (Liu et al. 2015b; Lu et al. 2015). It is also different from that in the flow of strongly shear-thinning and strongly viscoelastic HA solution, where in a straight square microchannel the larger particles migrate towards the channel centerline and the smaller ones migrate towards the vicinity of the walls (Del Giudice et al. 2017). In a straight rectangular microchannel, the particles' behaviors in HA solutions (Nam et al. 2019) become similar to those in PEO solutions (Li et al. 2016b).

4.1.1 Effect of flow rate

Figure 4a shows the composite images of 10 μm and 15 μm particles in 2000 ppm XG solution at the outlet expansion of a 30 μm deep microchannel under varying flow rates (see the original superimposed images of each type of particles in Fig. S-2). For flow rates less than 0.1 mL/h, the impact of inertial focusing is negligible because of the very small value of Re = 0.05. The consequence of rheological focusing is to direct particles towards the center and corners of the channel cross section. However, we find that the migration is sensitive to particle size in our experiment. Specifically, the majority of 15 μm particles travel adjacent to the channel walls leaving very few dispersed in the bulk of the microchannel. In contrast, most of 10 μm particles are focused into a tight stream along the channel centerline with the remainder close to the channel walls. Increasing the flow rate to 0.4 mL/h (Re = 0.4) completely depletes 15 μm particles from the bulk of the microchannel, and broadens the stream of 10 μm particles around the channel centerline. Further increasing the flow rate causes a displacement of 10 μm particles from the middle of the central stream to its edges. This movement eventually leads to a split of the central stream into two sub-streams at 4.0 mL/h (Re = 8.5), whose respective positions shift further towards the walls when the flow rate is increased to 6.0 mL/h. Therefore, 15 μm particles can be continuously separated from 10 μm particles in a wide range of flow rates, because they remain near the channel walls over the entire range of flow rates (Fig. 4a).

We also performed a control experiment in DI water in the same microchannel, and found that 10 μm and 15 μm particles are both focused towards the channel center though at different extents. Such an inertial focusing is a strong

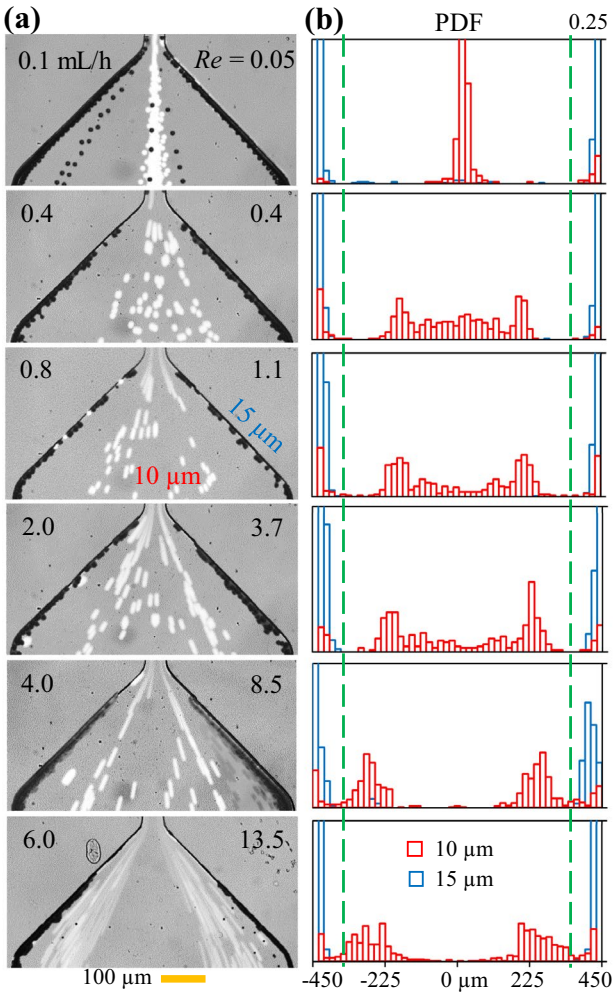

Fig. 4 Flow rate effect on the separation of 10 μm (bright) and 15 μm (dark) particles in 2000 ppm XG solution in a 65 μm wide and 30 μm deep rectangular microchannel: composite images (**a**) and particle PDF plots (**b**). The values of the experimentally imposed flow rate and the calculated Re are both labeled on the images. The two dashed lines on the PDF plots, which are each 100 μm away from the channel walls at the 900 μm-wide expansion region, divide the outlet expansion of the microchannel into the inner (for 10 μm particles) and outer (for 15 μm particles) zones for estimating the separation efficiency and purity of the two types of particles

function of flow rate [see the inertial force in Eq. (4)], and only becomes apparent for both types of particles when the flow rate reaches 4.0 mL/h (Re = 24.6) in our 2-cm-long microchannel (Fig. S-1). This observation is consistent with the previous studies in straight rectangular microchannels with a high aspect ratio (Liu et al. 2015a). We, therefore, predict that the rheological lift $\boldsymbol{F}_{rL}$ in 2000 ppm XG solution should dominate the inertial lift $\boldsymbol{F}_{iL}$, in the entire range of flow rates under test. Otherwise, either type of particle should exhibit an inward shift with the increase of flow rate. Referring to our earlier work on particle separation in PEO solutions (Li et al. 2016b), we propose to break down $\boldsymbol{F}_{rL}$

in XG solutions into two similar competing components: $\boldsymbol{F}_{\mathrm{rL}\to\mathrm{c}}$ directs particles towards the channel centerline and is small because of the weak elasticity of XG solutions; $\boldsymbol{F}_{\mathrm{rL}\to\mathrm{w}}$ directs particles towards the channel walls and is large because of the strong shear-thinning of XG solutions (Huang and Joseph 2000; Li et al. 2015). The particle behaviors in Fig. 4a indicate that $\boldsymbol{F}_{\mathrm{rL}\to\mathrm{w}}$ has a stronger effect on particle size and fluid flow rate than $\boldsymbol{F}_{\mathrm{rL}\to\mathrm{c}}$, which seems consistent with the scaling of the two lift components in PEO solutions (Li et al. 2016b).

Figure 4b shows the PDF plots of 10 μm and 15 μm particles for a quantitative comparison of their exiting positions at the channel outlet under varying flow rates, which were obtained directly from analyzing the particle images in Fig. 4a. The vertical axis in every plot has been limited to no more than 0.25, such that the PDF of 10 μm particles can be visually identified in the whole range of flow rates. The highest PDF value of 15 μm particles is greater than 0.3 in all plots. There is a clear separation between the two types of particles throughout the range of flow rates despite of a small region of overlap near the channel walls. We employ two metrics to evaluate this separation performance, which are the separation efficiency and purity as defined below:

$$\text{Efficiency} = \frac{\text{Number of targeted particles inside a specific zone}}{\text{Total number of targeted particles}}. \tag{7}$$

$$\text{Purity} = \frac{\text{Number of targeted particles inside a specific zone}}{\text{Total number of particles inside the same specific zone}}. \tag{8}$$

In our calculations the 900 μm-wide outlet expansion is split into an inner zone for 10 μm particles and an outer zone for 15 μm particles. The two division lines, as marked on the PDF plots in Fig. 4b, are each 100 μm away from the channel walls.

Figure 5 plots the two separation metrics for each type of particles. The separation efficiency of 15 μm particles in the outer zone is 100% except at the lowest flow rate of 0.1 mL/h (which is also 97%). In contrast, the separation efficiency of 10 μm particles in the inner zone is 92% at 0.1 mL/h and remains at roughly 85% from 0.4 to 6.0 mL/h. The separation purity of 10 μm particles in the inner zone is 100% except at 0.1 mL/h, because all 15 μm particles stay within the outer zone. The separation purity of 15 μm particles gradually reduces from 95% at 0.1 mL/h to 90% at 2.0 mL/h. However, it drops rapidly to 78% at 4.0 mL/h because of the split of the central 10 μm particle stream and further to 74% at 6.0 mL/h. We should note that the separation purity of 15 μm particles may be significantly biased by its relative total number to that of 10 μm particles. It is, therefore, safe to say that the two types of particles can

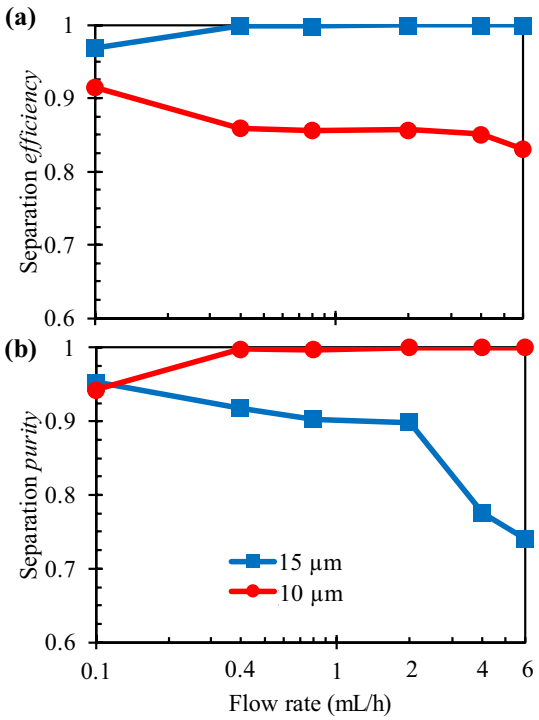

Fig. 5 Plots of the separation efficiency (**a**) and purity (**b**) for 10 μm and 15 μm particles in the flow of 2000 ppm XG solution through a 65 μm wide and 30 μm deep rectangular microchannel (determined from the PDF plots in Fig. 4b)

be effectively separated in the flow rate from 0.1 mL/h to at least 4.0 mL/h. This range spans nearly two orders of magnitude (precisely, 1.6 orders of magnitude), which is much wider than those reported sheath-free particle separations in the flow of viscoelastic solutions (regardless of the shear-thinning effect) (Liu et al. 2015b; Li et al. 2016b; Del Giudice et al. 2017; Nam et al. 2019) through straight rectangular microchannels.

4.1.2 Effect of XG concentration

Figure 6 shows the effect of XG concentration on the separation of 10 μm and 15 μm particles in a 30 μm deep microchannel under three selected flow rates: 0.1, 0.8, and 4.0 mL/h (see the particle images in a full range of flow rates in Figs. S-3 and S-4). Varying the XG concentration alters the fluid viscosity (see Fig. 1), leading to the variation of the Reynolds number (highlighted on the images of Fig. 6) and in turn the inertial lift. Moreover, it affects the fluid-dependent constants A and m and hence the rheological lift in Eq. (3). In 1000 ppm XG solution, nearly, all 15 μm particles line the channel walls at the outlet expansion as seen from the top-view images (Fig. 6a). Moreover, a greater

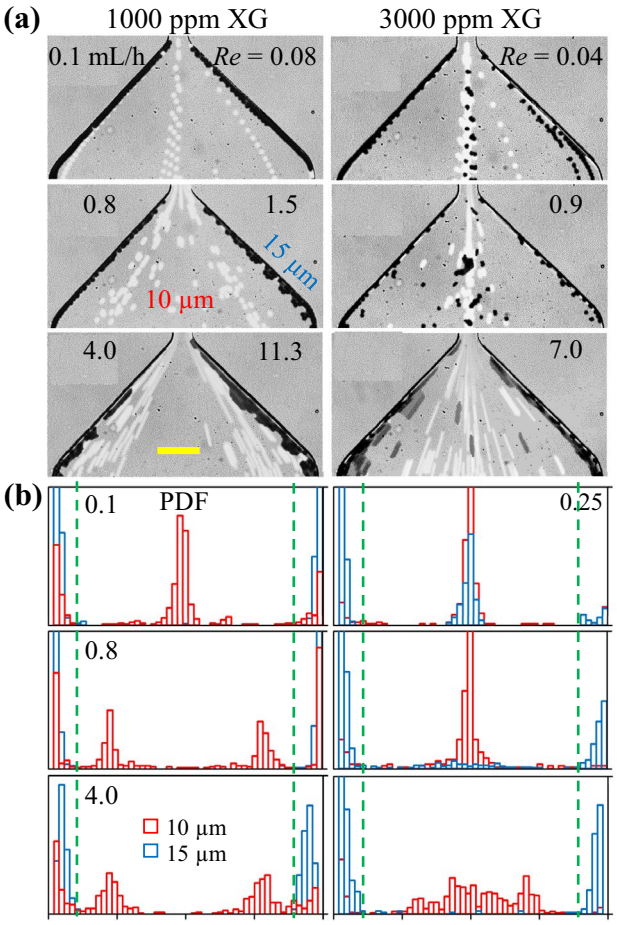

Fig. 6 Effect of XG concentration (left column, 1000 ppm; right column, 3000 ppm) on the separation of 10 μm (bright) and 15 μm (dark) particles in a straight 65 μm wide and 30 μm deep rectangular microchannel under selected flow rates: **a** composite images at the channel outlet with the values of flow rate and Re being both labeled; **b** corresponding particle PDF plots, where the two dashed lines (as defined in Fig. 4b) divide the outlet expansion into the inner and outer zones for 10 μm and 15 μm particles, respectively. The scale bar in **a** represents 100 μm

number of 10 μm particles appear adjacent to the channel wall than that in 2000 ppm XG solution (Fig. 4). These phenomena seem to suggest that the wall-directed component of the rheological lift $\boldsymbol{F}_{\mathrm{rL}\rightarrow\mathrm{w}}$, has a weaker dependence on the XG concentration than the center-directed one, $\boldsymbol{F}_{\mathrm{rL}\rightarrow\mathrm{c}}$, and hence decreases to a lesser extent in a lower concentration XG solution. This is further supported by the observation in 3000 ppm XG solution that 15 μm particles find an additional equilibrium position along the channel centerline at 0.1 mL/h because of the greater increase in $\boldsymbol{F}_{\mathrm{rL}\rightarrow\mathrm{c}}$ than $\boldsymbol{F}_{\mathrm{rL}\rightarrow\mathrm{w}}$ in a higher-concentration XG solution. This 15 μm particle central stream spreads and disappears with the increase of flow rate as a result of the larger relative increase of $\boldsymbol{F}_{\mathrm{rL}\rightarrow\mathrm{w}}$. Similar to the observation in Fig. 4, the central stream of 10 μm particles also spreads when the flow rate increases. Moreover, it splits into two near-wall sub-streams, for which the flow rate increases rapidly with the increase of XG concentration due to the stronger impact of $\boldsymbol{F}_{\mathrm{rL}\rightarrow\mathrm{c}}$. Specifically, the occurrence of dual near-wall particle streams takes place at 0.6 mL/h in 1000 ppm XG solution (Fig. S-3) as compared to 4.0 mL/h in 2000 ppm XG solution (Fig. 4). No division of the 10 μm particle central stream was observed in 3000 ppm XG solution for flow rates up to 6.0 ml/h (Fig. S-4). Overall, the separation of 10 μm and 15 μm particles gets worse when the XG concentration deviates from 2000 ppm.

4.1.3 Effect of channel depth

Figure 7a, b shows the composite images of 10 μm and 15 μm particles in 2000 ppm XG solution at the outlet expansion of 20 μm (AR = 3.3) and 54 μm (AR = 1.2) deep channels, respectively. In the shallower channel, both types of particles line up along the walls at the flow rate of 0.1 mL/h (Fig. 7a). These equilibrium positions do not vary for 15 μm particles under flow rates of up to 6.0 mL/h (Fig. S-5). In contrast, the exiting positions of 10 μm particles expand inward while still remaining adjacent to the channel walls in the whole range of flow rates under test. These phenomena may be attributed to two concurrent actions. One is the relative reduction in $\boldsymbol{F}_{\mathrm{rL}\rightarrow\mathrm{c}}$ as compared to $\boldsymbol{F}_{\mathrm{rL}\rightarrow\mathrm{w}}$ in a shallower microchannel, which causes the equilibrium particle position along the channel center to disappear. The other is the enhanced inertial lift, $\boldsymbol{F}_{\mathrm{iL}}$, which, though still weaker than $\boldsymbol{F}_{\mathrm{rL}\rightarrow\mathrm{w}}$ of 15 μm particles, may become comparable to that of 10 μm particles and hence shift them away from the channel walls when the flow rate increases. On the contrary, $\boldsymbol{F}_{\mathrm{rL}\rightarrow\mathrm{c}}$ increases relative to $\boldsymbol{F}_{\mathrm{rL}\rightarrow\mathrm{w}}$ in a deeper microchannel, leading to the formation of equilibrium positions at both the centerline and walls for 10 μm and 15 μm particles in the 54 μm deep channel (Fig. 7b). Moreover, the central stream of each type of particles broadens when the flow rate increases. However, the 15 μm particle stream is observed to first split into triple sub-streams at 0.8 mL/h and then dual near-wall sub-streams at 4.0 mL/h (Fig. S-6). These distinct particle behaviors in microchannels of varying depths are associated with the flow fields therein. As viewed from the shear rate distributions over the channel cross section in Fig. 7c (obtained from a 3D simulation of the flow of XG solution in real-sized rectangular microchannels using COMSOL®), the region with a negligible variation of shear rate is squeezed when the channel depth decreases.

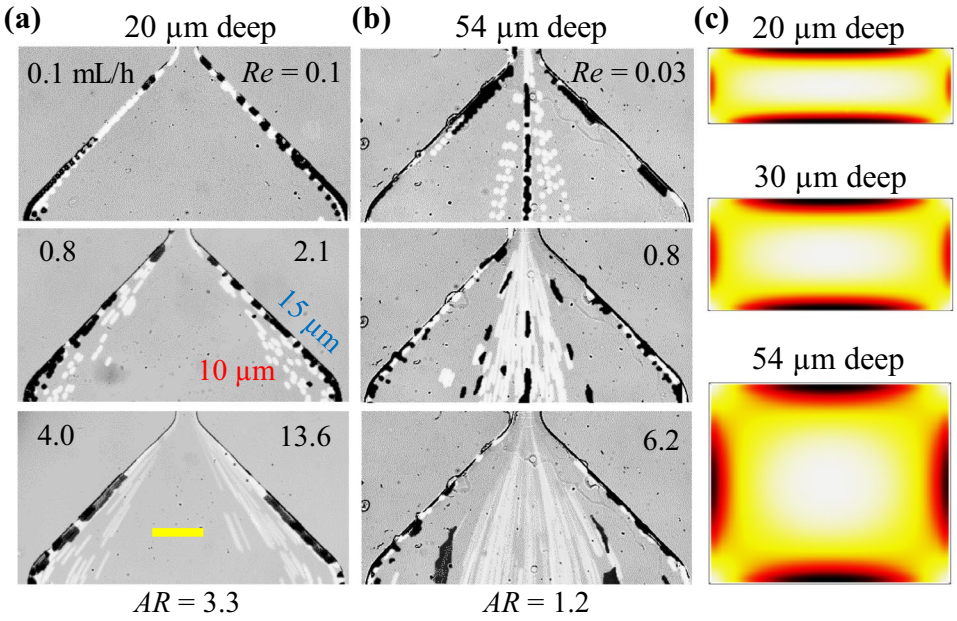

Fig. 7 Effect of channel depth (and hence the aspect ratio, AR) on the separation of 10 μm (bright) and 15 μm (dark) particles in 2000 ppm XG solution through a straight 65 μm wide rectangular microchannel under selected flow rates: **a** 20 μm deep with AR = 3.3; **b** 54 μm deep with AR = 1.2. **c** Shows the cross-sectional contours of fluid shear rate in microchannels of different depths. The scale bar represents 100 μm

4.2 Ternary particle separation

Figure 8 demonstrates a separation of 5 μm, 10 μm, and 15 μm particles in 2000 ppm XG solution through a 30 μm deep channel at the flow rate of 4.0 mL/h (see the particle images in a full range of flow rates in Fig. S-7). The relatively stronger dependence of $\boldsymbol{F}_{\mathrm{eL}\rightarrow\mathrm{w}}$ on particle size than $\boldsymbol{F}_{\mathrm{eL}\rightarrow\mathrm{c}}$ causes an inward shift of the equilibrium positions of particles when they get smaller. This explains why 5 μm particles form a relatively wide band around the channel centerline and leave only a small portion near the walls (Fig. 8b). Moreover, consistent with the binary separation of 10 μm and 15 μm particles at 4.0 mL/h in Fig. 3, the majority of 10 μm particles stay at the two near-wall equilibrium positions, while 15 μm particles still line the channel walls (Fig. 8a). To evaluate the performance of this ternary separation from the particle PDF plot in Fig. 8c, we divide the outlet expansion into the inner, middle, and outer zones for estimating the separation purity and efficiency of 5 μm, 10 μm, and 15 μm particles, respectively. The division lines between the middle and outer zones are the same as those in Fig. 4 for the binary particle separation. Those between the middle and inner zones are each set to 150 μm off the channel centerline. The calculated separation metrics for the three types of particles are presented in Table 2. The separation efficiency has the lowest value of 73% for 10 μm particles in the middle zone. The separation purity has the lowest value of 68% for 15 μm particles in the outer zone because of the occurrence of both 5 μm and 10 μm particles near the channel walls.

5 Conclusions

We have demonstrated for the first time that rigid spherical particles can be continuously separated by size in the flow of strongly shear thinning and weakly elastic XG solutions through straight rectangular microchannels. This sheath- and label-free particle separation results from the differential rheological focusing in XG solutions, where the larger particles line the channel walls and the smaller ones travel in the bulk of the microchannel. These particle migrations are fundamentally different from those reported in viscoelastic solutions because of the unique rheology of XG solutions, i.e., strongly shear thinning with little elasticity. We have also performed a comprehensive parametric study of the effects of flow rate, XG concentration, and channel depth on particle separation in XG solutions. Moreover, we have proposed to break down the fluid rheology-induced lateral force into a weak center-directed component, because of the weak elasticity of XG solutions, and a strong wall-directed component, because of the strong shear thinning of XG solutions. The competition between these two components explains qualitatively the observed shifting of particle focusing positions in the parametric study. It is important to note that our proposed sheath-free separation in XG solutions remains effective over a much wider range of flow rates (where the value of Re spans more than two orders of magnitude from 0.05 to ~ 10) than those reported in the flow of viscoelastic solutions (Lu et al. 2017; Yuan et al. 2018). This significant feature is envisioned to find both low and high throughput applications for the proposed particle separation in

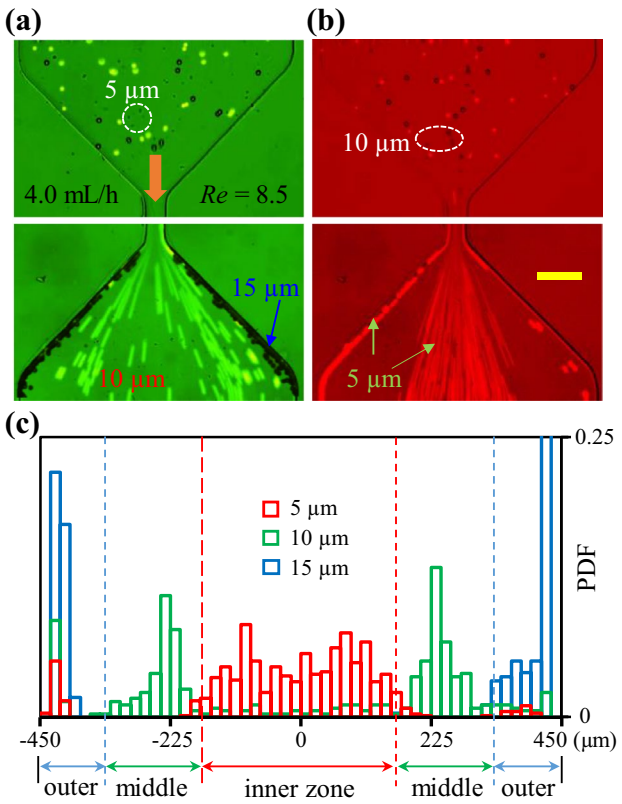

Fig. 8 Separation of 5 µm (red fluorescent), 10 µm (green fluorescent) and 15 µm (plain) spherical particles in 2000 ppm XG solution through a straight 65 µm wide and 30 µm deep rectangular microchannel at a flow rate of 4.0 mL/h: **a** snapshot image of all three types of particles at the channel inlet and composite image of 10 µm/15 µm particles at the channel outlet (both with a green filter); **b** snapshot image of all three types of particles at the channel inlet and superimposed image of 5 µm particles at the channel outlet (both with a red filter); **c** particle PDF plot, where the dashed lines divide the outlet expansion into the inner, middle and outer zones for estimating the separation efficiency and purity of 5 µm, 10 µm and 15 µm particles, respectively. The scale bar on the image in **b** represents 100 µm (color figure online)

Table 2 Estimated efficiency and purity of the ternary particle separation in Fig. 7

Particles (µm)	Number counts	Collecting zone	Efficiency (%)	Purity (%)
5	761	Inner zone	80	94
10	359	Middle zone	73	75
15	279	Outer zone	99	68

XG solutions. We will study in future work how this separation approach works for biological cells whose shape and deformability may each affect their equilibrium positions.

Acknowledgements This work was supported in part by Clemson University through a SEED Grant (XX), and by NSF under Grant Number CBET-1750208 (JB).

References

Ahn SW, Lee SS, Lee SJ, Kim JM (2015) Microfluidic particle separator utilizing sheathless elasto-inertial focusing. Chem Eng Sci 126:237–243

Amini H, Lee W, Di Carlo D (2014) Inertial microfluidic physics. Lab Chip 14:2739–2761

Asmolov ES (1999) The inertial lift on a spherical particle in a plane Poiseuille flow at large channel Reynolds number. J Fluid Mech 381:63–87

Aytouna M, Paredes J, Shahidzadeh-Bonn N, Moulinet S, Wagner C, Amarouchene Y, Eggers J, Bonn D (2013) Drop formation in non-Newtonian fluids. Phys Rev Lett 110:034501

Barnes HA, Hutton JF, Walters K (1989) An introduction to rheology. Elsevier, Amsterdam

Bird RB, Armstrong RC, Hassager O (1987) Dynamics of polymeric liquids, vol 1. Wiley, Hoboken

D'Avino G, Maffettone PL (2015) Particle dynamics in viscoelastic liquids. J Non-Newton Fluid Mech 215:80–104

D'Avino G, Greco F, Maffettone PL (2017) Particle migration due to viscoelasticity of the suspending liquid and its relevance in microfluidic devices. Annu Rev Fluid Mech 49:341–360

Del Giudice F, Sathish S, D'Avino G, Shen AQ (2017) "From the edge to the center": viscoelastic migration of particles and cells in a strongly shear-thinning liquid flowing in a microchannel. Anal Chem 89:13146–13159

Dhahir SA, Walters K (1989) On Non-Newtonian flow past a cylinder in a confined flow. J Rheol 33:781–804

Escudier MP, Smith S (1999) Turbulent flow of Newtonian and shear-thinning liquids through a sudden axisymmetric expansion. Exp Fluid 27:427–434

Gossett DR, Weaver WM, Mach AJ, Hur SC, Tse HT, Lee W, Amini H, Di Carlo D (2010) Label-free cell separation and sorting in microfluidic systems. Anal Bioanal Chem 397:3249–3267

Ha B, Park J, Destgeer G, Jung JJ, Sung HJ (2016) Transfer of microparticles across laminar streams from non-Newtonian to Newtonian fluid. Anal Chem 88:4205–4210

Haase AS, Wood JA, Sprakel LM, Lammertink RG (2017) Inelastic non-Newtonian flow over heterogeneously slippery surfaces. Phys Rev E 95:023105

Haward SJ, Jaishankar A, Oliveira MSN, Alves MA, McKinley GH (2013) Extensional flow of hyaluronic acid solutions in an optimized microfluidic cross-slot device. Biomicrofluid 7:044108

Ho BP, Leal LG (1974) Inertial migration of rigid spheres in two-dimensional unidirectional flows. J Fluid Mech 65:365–400

Huang PY, Joseph DD (2000) Effects of shear thinning on migration of neutrally buoyant particles in pressure driven flow of Newtonian and viscoelastic fluids. J Non-Newton Fluid Mech 90:159–185

Japper-Jaafar A, Escudier MP, Poole RJ (2010) Laminar, transitional and turbulent annular flow of drag-reducing polymer solutions. J Non-Newton Fluid Mech 165:1357–1372

Kang K, Lee SS, Hyun K, Lee SJ, Kim JM (2013) DNA-based highly tunable particle focuser. Nat Commun 4:2567

Karimi A, Yazdi S, Ardekani AM (2013) Hydrodynamic mechanisms of cell and particle trapping in microfluidics. Biomicrofluid 7:021501

Lapizco-Encinas BH (2019) On the recent developments of insulator-based dielectrophoresis: a review. Electrophoresis 40:358–375

Leal LG (1979) The motion of small particles in non-Newtonian fluids. J Non-Newton Fluid Mech 5:33–78
Leal LG (1980) Particle motions in a viscous fluid. Annu Rev Fluid Mech 12:435–476
Lee DJ, Brenner H, Youn JR, Song YS (2013) Multiplex particle focusing via hydrodynamic force in viscoelastic fluids. Sci Rep 3:3258
Leshansky AM, Bransky A, Korin N, Dinnar U (2007) Tunable nonlinear viscoelastic "focusing" in a microfluidic device. Phys Rev Lett 98:234501
Li D, Xuan X (2018) Fluid rheological effects on particle migration in a straight rectangular microchannel. Microfluid Nanofluid 22:49
Li D, Xuan X (2019) The motion of rigid particles in the Poiseuille flow of pseudoplastic fluids through straight rectangular microchannels. Microfluid Nanofluid 23:54
Li G, McKinley GH, Ardekani AM (2015) Dynamics of particle migration in channel flow of viscoelastic fluids. J Fluid Mech 785:486–505
Li D, Lu X, Song Y, Wang J, Li D, Xuan X (2016a) Sheathless electrokinetic particle separation in a bifurcating microchannel. Biomicrofluid 10:054104
Li D, Lu X, Xuan X (2016b) Viscoelastic separation of particles by size in straight rectangular microchannels: a parametric study for a refined understanding. Anal Chem 88:12303–12309
Li D, Zielinski J, Kozubowski L, Xuan X (2018) Continuous sheath-free separation of drug-treated human fungal pathogen *Cryptococcus Neoformans* by morphology in biocompatible polymer solutions. Electrophoresis 39:2362–2369
Lim H, Nam J, Shin S (2014) Lateral migration of particles suspended in viscoelastic fluids in a microchannel flow. Microfluid Nanofluid 17:683–692
Lindner A, Bonn D, Meunier J (2000) Viscous fingering in a shear-thinning fluid. Phys Fluid 12:256–261
Liu C, Hu G (2017) High-throughput particle manipulation based on hydrodynamic effects in microchannels. Micromachines 8:73
Liu C, Hu G, Jiang X, Sun J (2015a) Inertial focusing of spherical particles in rectangular microchannels over a wide range of Reynolds numbers. Lab Chip 15:1168–1177
Liu C, Xue C, Chen X, Shan L, Tian Y, Hu G (2015b) Size-based separation of particles and cells utilizing viscoelastic effects in straight microchannels. Anal Chem 87:6041–6048
Liu C, Ding B, Xue C, Tian Y, Hu G, Sun J (2016) Sheathless focusing and separation of diverse nanoparticles in viscoelastic solutions with minimized shear thinning. Anal Chem 88:12547–12553
Liu C, Guo J, Tian F, Yang N, Yan F, Ding Y, Wei J, Hu G, Nie G, Sun J (2017) Field-free isolation of exosomes from extracellular vesicles by microfluidic viscoelastic flows. ACS Nano 11:6968–6976
Liu C, Zhao J, Tian F, Chang J, Zhang W, Sun J (2019) λ-DNA and aptamer mediated sorting and analysis of extracellular vesicles. J Am Chem Soc 141:3817–3821
Lu X, Xuan X (2015a) Continuous microfluidic particle separation via elasto-inertial pinched flow fractionation. Anal Chem 87:6389–6396
Lu X, Xuan X (2015b) Elasto-inertial pinched flow fractionation for continuous shape-based particle separation. Anal Chem 87:11523–11530
Lu X, Zhu L, Hua RM, Xuan X (2015) Continuous sheath-free separation of particles by shape in viscoelastic fluids. Appl Phys Lett 107:264102
Lu X, Liu C, Hu G, Xuan X (2017) Particle manipulations in non-Newtonian microfluidics: a review. J Colloid Interface Sci 500:182–201
Martel JM, Toner M (2014) Inertial focusing in microfluidics. Annu Rev Biomed Eng 16:371–396
Munaz A, Shiddiky MJA, Nguyen NT (2018) Recent advances and current challenges in magnetophoresis based micro magnetofluidics. Biomicrofluid 12:031501
Nam J, Lim H, Kim D, Jung H, Shin S (2012) Continuous separation of microparticles in a microfluidic channel via the elasto-inertial effect of non-Newtonian fluid. Lab Chip 12:1347–1354
Nam J, Namgung B, Lim CT, Bae JE, Leo HL, Cho KS, Kim S (2015a) Microfluidic device for sheathless particle focusing and separation using a viscoelastic fluid. J Chromatogr A 1406:244–250
Nam J, Tan JK, Khoo BL, Namgung B, Leo HL, Lim CT, Kim S (2015b) Hybrid capillary-inserted microfluidic device for sheathless particle focusing and separation in viscoelastic flow. Biomicrofluid 9:064117
Nam J, Shin Y, Tan JKS, Lim YB, Lim CT, Kim S (2016) High-throughput malaria parasite separation using a viscoelastic fluid for ultrasensitive PCR detection. Lab Chip 16:2086–2092
Nam J, Jang WS, Hong DH, Lim CS (2019) Viscoelastic separation and concentration of fungi from blood for highly sensitive molecular diagnostics. Sci Rep 9:3067
Rodd LE, Scott TP, Boger DV, Cooper-White JJ, McKinley GH (2005) The inertio-elastic planar entry flow of low-viscosity elastic fluids in micro-fabricated geometries. J Non-Newton Fluid Mech 129:1–22
Sajeesh P, Sen AK (2014) Particle separation and sorting in microfluidic devices: a review. Microfluid Nanofluid 17:1–52
Stoecklein D, Di Carlo D (2019) Nonlinear microfluidics. Anal Chem 91:296–314
Tang W, Jiang D, Li Z, Zhu L, Shi J, Yang J, Xiang N (2019) Recent advances in microfluidic cell sorting techniques based on both physical and biochemical principles. Electrophoresis 40:930–954
Tian F, Zhang W, Cai L, Li S, Hu G, Cong Y, Liu C, Li T, Sun J (2017) Microfluidic co-flow of Newtonian and viscoelastic fluids for high-resolution separation of microparticles. Lab Chip 17:3078–3085
Tian F, Cai L, Chang J, Li S, Liu C, Li T, Sun J (2018) Label-free isolation of rare tumor cells from untreated whole blood by interfacial viscoelastic microfluidics. Lab Chip 18:3436–3445
Tian F, Feng Q, Chen Q, Liu C, Li T, Sun J (2019) Manipulation of bio-micro/nanoparticles in non-Newtonian microflows. Microfluid Nanofluid 23:68
Villone MM, D'Avino G, Hulsen MA, Greco F, Maffettone PL (2013) Particle motion in square channel flow of a viscoelastic liquid: migration vs. secondary flows. J Non Newton Fluid Mech 195:1–8
Won D, Kim C (2004) Alignment and aggregation of spherical particles in viscoelastic fluid under shear flow. J Non-Newton Fluid Mech 117:141–146
Wu M, Ozcelik A, Rufo J, Wang Z, Fang R, Huang TJ (2019) Acoustofluidic separation of cells and particles. Microsyst Nanoeng 5:32
Wyatt NB, Liberatore MW (2009) Rheology and viscosity scaling of the polyelectrolyte xanthan gum. J Appl Polymer Sci 114:4076–4084
Yan S, Zhang J, Yuan D, Li W (2017) Hybrid microfluidics combined with active and passive approaches for continuous cell separation. Electrophoresis 38:238–249
Yang S, Kim JY, Lee SJ, Lee SS, Kim JM (2011) Sheathless elasto-inertial particle focusing and continuous separation in a straight rectangular microchannel. Lab Chip 11:266–273
Yang S, Lee SS, Ahn SW, Kang K, Shim W, Lee G, Hyun K, Kim JM (2012) Deformability-selective particle entrainment and separation in a rectangular microchannel using medium viscoelasticity. Soft Matter 8:5011–5019
Yasuda K, Armstrong RC, Cohen RE (1981) Shear flow properties of concentrated solutions of linear and star branched polystyrenes. Rheol Acta 20:163–178

Yuan D, Zhang J, Yan S, Peng G, Zhao Q, Alici G, Du H, Li W (2016a) Investigation of particle lateral migration in sample-sheath flow of viscoelastic fluid and Newtonian fluid. Electrophoresis 37:2147–2155

Yuan D, Zhang J, Sluyter R, Zhao Q, Yan S, Alicia G, Li W (2016b) Continuous plasma extraction under viscoelastic fluid in a straight channel with asymmetrical expansion–contraction cavity arrays. Lab Chip 16:3919–3928

Yuan D, Tan S, Sluyter R, Zhao Q, Yan S, Nguyen NT, Guo J, Zhang J, Li W (2017a) On-chip microparticle and cell washing using coflow of viscoelastic fluid and newtonian fluid. Anal Chem 89:9574–9582

Yuan D, Tan S, Zhao Q, Yan S, Sluyter R, Nguyen NT, Zhang J, Li W (2017b) Sheathless dean-flow-coupled elasto-inertial particle focusing and separation in viscoelastic fluid. RSC Adv 7:3461–3469

Yuan D, Zhao Q, Yan S, Tang SY, Alici G, Zhang J, Li W (2018) Recent progress of particle migration in viscoelastic fluids. Lab Chip 18:551–567

Zhang J, Yan S, Yuan D, Alici G, Nguyen NT, Warkiani ME, Li W (2016) Fundamentals and applications of inertial microfluidics: a review. Lab Chip 16:10–34

Zhou Y, Ma Z, Tayebi M, Ai Y (2019) Submicron particle focusing and exosome sorting by wavy microchannel structures within viscoelastic fluids. Anal Chem 91:4577–4584

Zirnsak MA, Boger DV, Tirtaatmadja V (1999) Steady shear and dynamic rheological properties of xanthan gum solutions in viscous solvents. J Rheol 43:627–650